Quantitative analysis of aligned molecule photoelectron angular distributions

Joanne L. Woodhouse[1*], James O. F. Thompson[2,3], Jakub Benda[4], Richard T. Chapman[3], Paul Hockett[5], Varun Makhija[6], Zdeněk Mašín[4], Katharine L. Reid[2], Emma Springate[3], Adam S. Wyatt[3], Yu Zhang[3] and Russell S. Minns[1**]

[1] *School of Chemistry and Chemical Engineering, University of Southampton, Highfield, Southampton SO17 1BJ, U.K.**

[2] *School of Chemistry, The University of Nottingham, University Park, Nottingham NG7 2RD, U.K.*

[3] *Central Laser Facility, STFC Rutherford Appleton Laboratory, Didcot, Oxfordshire OX11 0QX, U.K.*

[4] *Institute of Theoretical Physics, Faculty of Mathematics and Physics, Charles University, V Holešovičkách 2, 180 00 Prague 8, Czechia*

[5] *National Research Council, 100 Sussex Drive, Ottawa, Ontario K1A 0R6, Canada and*

[6] *Department of Chemistry and Physics, University of Mary Washington, Fredericksburg, VA 22401, USA*

(Dated: February 5, 2025)

Molecular frame photoelectron angular distributions (MFPADs) provide the full available detail of the photoionization process. Careful analysis of the evolving photoelectron angular distribution during the coherent rotation of a non-adiabatically aligned sample of molecules allows the detail which is smoothed out by orientational averaging in the laboratory frame to be resolved. Here we exploit a novel high flux monochromated HHG lightsource to provide single-photon photoelectron angular distributions of field-free aligned molecules. Our measurements are sensitive to alignment frame variations in even β_n parameters up to n=6 in the PADs of the first four ionization channels of OCS, allowing for rigorous benchmarking of the cutting edge theoretical methods used for simulation of MFPADs. We demonstrate that experimentally derived molecular alignment distributions may be combined with theoretical MFPADs to generate theoretical alignment-frame PADs which provide a quantitative comparison to the experimental β_n parameters. The experimental data and ePSproc simulated PADs show quantitative agreement and sensitivity to picometer-scale changes in the molecular geometry. This combined methodology therefore provides a versatile way of studying geometry-sensitive continuum structural features for non-dissociative ionization processes which may not be studied in the recoil frame. These measurements therefore provide a strict test of the theoretical descriptions and will stand as benchmark measurements for future comparisons to higher level theory.

I. INTRODUCTION

When a molecule is ionized by the absorption of photons, the partial waves which comprise the photoelectron wavefunction, and their relative phases, are determined by the symmetry of electronic states of the molecule and ionization continuum as well as scattering by the molecular potential.[1–7] As a result, the observed photoelectron partial wave interference pattern is dependent on both the symmetry of the ionization transition and the molecular geometry. If photoelectron spectroscopy measurements were performed in the molecular frame, the full detail of the ionization and electron scattering process could be revealed, however, much of this information is lost in traditional photoelectron spectroscopy experiments where the random orientation of molecules in the sample causes the observed photoelectron signal to be an average of multiple ionization and scattering processes. For ionization which results in prompt dissociation and fragment recoil along the axes of the bonds being broken, this orientational averaging may be overcome by using a coincidence spectrometer to correlate the momentum vectors of photoelectrons and their corresponding ionic fragments and produce a recoil-frame photoemission spectrum.[8–15] Photoelectron-photoion coincidence spectroscopy has been used to fully retrieve molecular frame information and even to image a polyatomic molecule,[16] however, as the analysis of recoil frame data relies on the axial recoil approximation, this approach cannot be applied to ionization events that either do not lead to dissociation or where the ionized molecule has time to bend or rotate prior to fragmentation.[17]

Alternatively, aligning molecules in space prior to ionization would allow the molecular axis along which ionization takes place to be selected and therefore the photoelectron angular distribution (PAD) to be measured for a single ionization transition. Full analysis of the PAD from even partially aligned samples can yield detailed information on the photoionization event, and so-called 'complete' experiments, where the magnitude and relative phases of the radial dipole matrix elements for ionization are extracted from experimental data, have been successfully carried out using nanosecond 2+1 REMPI photoelectron imaging, which took advantage of the transient alignment of photoexcited molecules and the relatively narrow bandwidth of nanosecond laser systems to produce rotationally-resolved photoelectron images with angular momentum components up to L=6.[18] Femtosecond 1+1' REMPI experiments have also achieved this through monitoring the PAD as the molecular axis distri-

* j.l.woodhouse@soton.ac.uk; r.s.minns@soton.ac.uk

bution evolves over time between the excitation and ionization pulses.[19] However, the necessity for rotational resolution limits the application of these techniques to relatively small molecular systems as well as to ionization from electronically excited states. Through the advent of impulsive alignment techniques, [20, 21] it has become possible that the same level of detail may be recovered for a non-dissociative ground state ionization process by allowing the ionization of a highly aligned sample of molecules in field-free conditions.[22–26]

While the information contained in the PADs of oriented molecules has been recognized for many years,[27] the limitations of the alignment techniques and light sources available has largely prevented these measurements from being carried out. Synchrotron sources have been used to record the PADs of many molecules over wide energy ranges,[28, 29] but the long pulse duration of synchrotron radiation makes such measurements incompatible with field-free alignment techniques, which achieve transient alignment for short periods on the order of hundreds of femtoseconds. The use of ultrafast laser systems has allowed for the measurement of PADs from molecules aligned using field-free impulsive alignment techniques,[30] however, many benchtop ultrafast laser systems deliver wavelengths in the infrared to ultraviolet ranges such that multiple photons must be used to exceed the molecular ionization energy. As the PAD is determined by the electronic state occupied by the molecule prior to ionization, the increased likelihood of hitting resonant intermediate states when using multiphoton or resonant multiple photon ionization schemes complicates the interpretation of results and limits the range of energies over which experiments may be performed.

New light sources, such as X-ray free electron lasers (XFELs), have been used to record single-wavelength photoelectron spectra of aligned molecules in the soft X-ray range, however, the wavelength instability of free electron laser sources based on unseeded self amplified spontaneous emission (SASE) limited the energy resolution of the photoelectron images.[31] XFELs which are either externally seeded for High Gain Harmonic Generation (HGHG) or self-seeded by filtered SASE radiation in the amplification stage achieve greater coherence and wavelength stability relative to unseeded SASE XFELs and therefore provide a promising route to improving the resolution of photoelectron images for alignment frame experiments in the XUV to X-ray ranges.[32, 33]

Of most relevance to the present study are high harmonic generation (HHG) sources, which can yield attosecond-to-femtosecond pulses of extreme ultraviolet (XUV) light and have allowed for the measurement of PADs of several molecules (O_2, N_2, CO, CO_2 and CF_3I) aligned in field-free conditions.[23, 34–38] However, due to the low flux of HHG sources and the complexity of monochromation, these experiments used the full frequency comb yielded by the HHG process, leading in most cases to highly congested spectra with multiple overlapping bands from which quantitative PAD measurements could not be obtained. Previous alignment frame PAD (AFPAD) measurements on N_2 made use of spread out filtered harmonics from a UV drive wavelength which allowed for matrix element retrieval and reconstruction of molecular frame PADs for the $\tilde{X}$, $\tilde{A}$ and $\tilde{B}$ channels for comparison with theoretical MF-PADs, though no quantitative comparison between the experimental observables and theory was explored in that work.[23] Additionally, the contribution of high energy harmonics to the spectrum limits the resolution of images and typically presents issues with using cold (seeded) molecular beams due to background signal from ionization of the carrier gas.[23]

We present the first alignment frame photoelectron spectroscopy measurements using monochromated extreme ultraviolet light[39] from a HHG light source. We note that a similar experimental configurations have previously been used to investigate PADs from time-overlapped XUV and IR pulses [40], but not to measure field-free alignment-frame PADs; in general such experiments are desirable, but very challenging due to the statistics required for high-fidelity PAD measurements, and concomitant requirements for high HHG flux and stability. Using a single isolated harmonic allowed for quantitative measurement of anisotropy parameters by minimising overlapping bands in the spectra, also allowing us to separate out contributions from the $\tilde{A}^2\Pi_u$ and $\tilde{B}^2\Sigma_u^+$ channels which lie very close together in energy. We extract the time-dependent alignment moments from our experimental photoelectron yield data[23–25] and combine these with photoelectron scattering calculations to reproduce the evolution of the PAD as the molecular axis distribution changes, providing an experimental benchmark for photoelectron scattering calculations which quantitatively model the molecular frame PAD.

II. EXPERIMENTAL METHODOLOGY

The OCS/He beam is created via supersonic expansion of a mixture of 2% OCS in He at 700 mbar through a 1 kHz pulsed Amsterdam valve, 75 mm away from a 300 μm diameter skimmer. The collimated molecular beam intersects perpendicularly with the laser at the centre of a velocity map imaging spectrometer. The fundamental output of a Ti:Sapphire amplified laser system (Red Dragon, KMLabs) is divided into two arms, the pump arm and probe arm. For the alignment (pump) arm, the 790 nm fundamental is stretched by retroreflection within a 60 mm N-BK7 right-angle prism to a pulse duration of 300 fs, and the pulse energy is attenuated to 300 μJ. The probe arm was redirected through different optical pathways to generate either an 800 nm Coulomb explosion probe pulse for quantification of the molecular alignment or an XUV probe pulse for photoelectron spectroscopy measurements.

For the Coulomb explosion measurements, the polar-

ization of the probe arm is rotated by 90° to lie perpendicular to the detector plane by passing through a $\lambda/2$ waveplate, such that the anisotropy of the Coulomb explosion signal does not artificially enhance the apparent alignment in the Coulomb explosion images,[41] meaning that the alignment measured from the anisotropy of the Coulomb explosion images is a lower limit of the achieved alignment of OCS. The alignment pulse polarization was set to lie in the plane of the detector. The Coulomb explosion pulse is then recombined with the stretched pump arm, and the power is attenuated to 500 μJ outside of the chamber, with 50 fs pulse duration. Both Coulomb explosion and alignment arms are focussed collinearly into the interaction region of a velocity map imaging spectrometer using a 1.2 m focal length lens resulting in a focal spot size of ∼120 μm. The MCP detector is gated to select for an m/z of 16, resulting in images of O^+ and S^{2+} ions formed by Coulomb explosion. 60 images were recorded between 38 ps - 44 ps delay relative to the alignment pulse in order to capture the first rotational revival of OCS. The images were integrated over 200000 laser shots and alignment was quantified in terms of $\cos^2\theta_{2D}$ by calculating the overlap integral of the radially integrated high KE signal with a $\cos^2\theta$ function, as the high KE signal has minimal overlap with the unaligned Coulomb explosion and dissociative ionization signal at the centre of the image.

For the photoelectron spectroscopy measurements the probe is generated via high harmonic generation using approximately 500 μJ of the fundamental of the Red Dragon output at 790 nm. The 15th harmonic (52.5 nm, 23.6 eV) or 13th harmonic (60.5 nm, 20.5 eV) is isolated using a time-preserving monochromator and reflection focused off a toroidal mirror into the interaction chamber. Overlap between the two laser pulses is ensured with the use of a scintillator crystal located at the centre of the VMI spectrometer and optimized on the photoelectron signal from ionization of argon at t_0. The FWHM $\Delta E/E$ kinetic energy resolution of the velocity map images is approximately 10 % eKE measured from direct ionization of argon with HH15 and HH13. Both alignment and XUV beams are linearly polarized in the plane of the MCP detector and cross at an angle of approximately 3°. Rotation of the polarization of the alignment pulse using a $\lambda/2$ waveplate allowed for measurements of photoelectron spectra with OCS molecules aligned and antialigned with respect to the polarization of the ionizing XUV pulse. The XUV pulse polarization was in the detector plane for all measurements.

The photoelectron spectra of aligned and antialigned molecules were recorded for 600000 laser shots at a delay time of 40.5 ps, i.e. at the peak of the first rotational revival of OCS. Alignment-dependent PADs were also measured by recording a series of 61 photoelectron images, each recorded for 360000 laser shots in the range 38 - 44 ps, covering the first rotational revival of OCS. Images of background scatter from the XUV and ionization by the alignment pulse were recorded and subtracted from the pump-probe images. The photoelectron images were inverted using the polar onion peeling (POP) algorithm[42] fitting with even order Legendre polynomials. Fits were carried out including Legendre polynomials up to β_{10}, but there was no significant intensity observed for β_8 and β_{10}, so the fitting function for the presented results was truncated at β_6. Experimental errors for the time-dependent photoelectron yields and β_n values were calculated as the standard deviation of the values at baseline, where the distribution of molecular axes can be considered approximately constant. For the laboratory frame β_n values, errors are calculated as the standard deviation in β_n values across the kinetic energy range of the peak. The eKE distributions were independently calibrated using photoelectron images from direct ionization and ATI of Argon at t_0 between the alignment and ionization pulses and the known ionization energy of Argon (15.759 eV).

III. THEORETICAL METHODOLOGY

A. Extraction of molecular axis distribution moments

A full discussion of axis retrieval in the context of PADs can be found in Ref. [26]. In brief, in the case of a time-resolved measurement of a scalar observable S from a rotational wavepacket, the quantum expectation value of S is given by the following expression,

$$\langle S\rangle(t) = \sum_{jk} C_{jk}\langle D^j_{0k}\rangle(t) \tag{1}$$

where C_{jk} are unknown expansion coefficients, and D^j_{0k} are the Wigner D-Matrix elements, a basis on the space of orientations. Since the rotational wavepacket can be accurately simulated, the $\langle D^j_{0k}\rangle(t)$ are considered known. Given a measured time resolved signal $\langle S\rangle(t)$, the unknown coefficients C_{jk} can be determined by linear regression, and the molecular frame signal determined. [43, 44].

For the case of photoionization from a time-dependent ensemble, an equivalent equation can be written in terms of the $\beta_{L,M}(\epsilon,t)$ parameters:

$$\beta_{L,M}(\epsilon,t) = \sum_{K,Q,S} \bar{C}^{LM}_{KQS}(\epsilon) A^K_{Q,S}(t) \tag{2}$$

where the $\beta_{L,M}(\epsilon,t)$ define the observable anisotropy parameters, the coefficients $\bar{C}^{LM}_{KQS}$ are unknowns which parameterize the dependence of the observables on the molecular alignment, and the alignment is defined by a set of axis distribution moments $A^K_{Q,S}(t)$. Again, the unknowns can be retrieved via linear regression with simulated rotational wavepackets. [23, 26, 45] In the current case, fitting indicated good agreement with experimental

results for an alignment pulse of 300 fs and peak intensity 4.2 TW, consistent with the experimental conditions, and a sample rotational temperature of 28 K.

B. Alignment Frame PAD Calculations

Computation of AFPADs made use of various tools:

1. Gamess was used for electronic structure computations [46–48]. Initial computations (HF/aug-cc-pVDZ) found equilibrium bond lengths of R_{C-S} = 1.60 Å, R_{C-O} = 1.16 Å, in reasonable agreement with experimental[49] (R_{C-S} = 1.56 Å, R_{C-O} = 1.16 Å) and MRSDCI reference calculations[50] (R_{C-S} = 1.57 Å, R_{C-O} = 1.16 Å). Single-point computations for a range of geometries with bonds stretched by a given percentage (relative to the equilibrium geometry) were also performed, as discussed below, consistent with stretched equilibrium geometries in various states of the molecular cation (hence broad Franck-Condon envelopes), see Refs. [50, 51] for general discussion.

2. Photoionization (continuum scattering) calculations made use of ePolyScat [52–55]. From a given electronic structure input file, dipole matrix elements were computed as a function of ionization channel (orbital and symmetry) and electron kinetic energy. Photoionization calculations based on a 20% stretched geometry (R_{C-S} = 1.85 Å, R_{C-O} = 1.39 Å) were found to agree well with room-temperature laboratory frame measurements from the literature (see Sect. IV C and Fig. 3, an extended presentation showing bond-length dependence can be found in the ESI, Fig. S4).

3. Computation of aligned-frame observables made use of the ePSproc suite [56, 57], which implements the computation of observables based on dipole matrix elements and the aligned frame axis distributions ($A^K_{Q,S}(t)$ parameters per Sect. III A).

The general methods outlined above are provided in detail in Refs. [26, 45]. In particular, note that the final observables (step 3 above), are computed herein using a tensor formalism:

$$\beta_{L,M}(\epsilon,t) = \sum_{\zeta,\zeta'} \Upsilon^{\zeta\zeta'}_{L,M}(t)\mathbb{I}^{\zeta\zeta'}(\epsilon) \tag{3}$$

Where $\Upsilon^{u,\zeta\zeta'}_{L,M}(t)$ are the channel functions, which include the required angular momentum and symmetry factors for a given ionizing transition and molecular alignment (set of $A^K_{Q,S}(t)$ parameters); $\mathbb{I}^{\zeta\zeta'}(\epsilon)$ are the dipole matrix elements, here obtained as per step 2 above. The terms are dependent on a set of quantum numbers which are collectively labelled ζ, and define all other required properties. A full set of data from the *ab initio* calculations and processing (as Jupyter notebooks) outlined above, and as presented herein (Sect. IV D), are available via Figshare.[58]

Finally, identification of possible vibrational effects is explored in the discussion of experimental results below (see, in particular, Sect. IV C). In this work, this is explored through comparison of experimental data in both the laboratory and alignment frames to calculations for a small representative sample of molecular geometries. A full vibrational wavefunction calculation and geometry sampling will be explored in future work. Nonetheless, the good agreement with the current single-geometry model and the experimental results suggest that such effects will be small in the current case, and the core photoionization physics can be reasonably well-modelled by a single-geometry treatment.

IV. RESULTS AND DISCUSSION

A. Coulomb explosion of aligned OCS

The degree of alignment of OCS molecules was quantified through the $\cos^2\theta_{2D}$ values of the images of O^+ and S^{2+} ions from Coulomb explosion of OCS, which are plotted in purple as a function of delay time following the NIR alignment pulse in Fig. 1. The Coulomb explosion images for the time delays of 38.0 ps, 40.5 ps, 41.6 ps and 44.0 ps are also presented in Fig. S1 in the ESI. It can be seen that the baseline value of $\cos^2\theta_{2D}$ is ∼0.58 c.f. 0.5 (the value of $\cos^2\theta_{2D}$ obtained from an isotropic distribution), indicating that the alignment pulse has induced long-lived alignment of OCS. This long-lived alignment can be seen in the oval shape of the Coulomb explosion images at 38.0 ps and 44.0 ps in Fig. S1, which correspond to the baseline before and after the first revival. The Coulomb explosion images recorded in the absence of the alignment pulse yield the expected value of $\cos^2\theta_{2D} = 0.5$. The values of $\cos^2\theta_{2D}$ increase to a maximum value of 0.72 at a delay of 40.5 ps, corresponding to a $\cos^2\theta_{3D}$ value of approximately 0.58. 40.5 ps therefore corresponds to the time delay at which the molecular axis distribution is most aligned with the polarization of the alignment pulse.

B. Alignment Frame Ionization Cross Sections

Photoelectron spectra were recorded at 23.6 eV for OCS molecules that were unaligned, aligned and antialigned with respect to the ionization pulse polarization, and are presented in Fig. 2 alongside the He(I) spectrum of OCS reproduced with permission from reference 59. At these wavelengths the first four ionization channels of OCS, $\tilde{X}^2\Pi_g$, $\tilde{A}^2\Pi_u$, $\tilde{B}^2\Sigma^+_u$ and $\tilde{C}^2\Sigma^+_g$, are accessible and it can be seen from Fig. 2 that the ionization

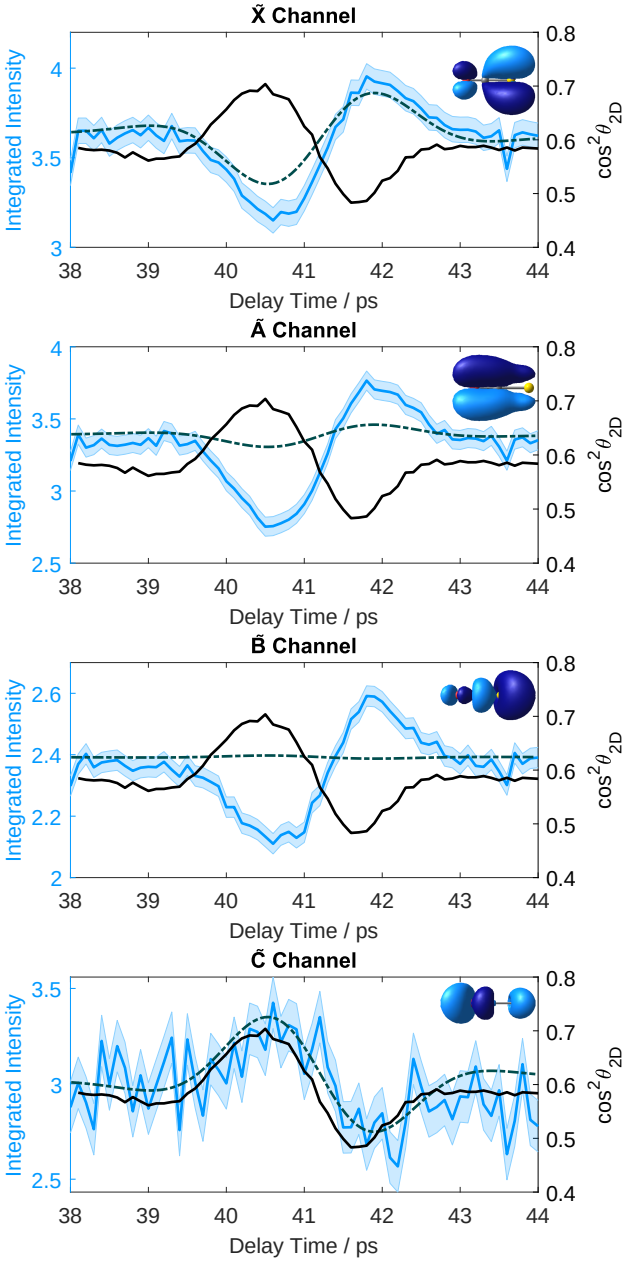

FIG. 1. Plots of experimental integrated photoelectron yields to the first four ionization channels of OCS as a function of pump-probe time delay (blue lines). The photoelectron yield values have been normalized to the scale of the ePSProc alignment frame cross sections (dashed dark green lines). Experimental values are averaged over the kinetic energy ranges which correspond to the widths of the four features in the photoelectron spectrum (eKEs = $\tilde{X}$: 12.0 - 12.4 eV, $\tilde{A}$: 8.1 - 8.7 eV $\tilde{B}$: 7.4 - 8.0 eV $\tilde{C}$: 5.7 - 5.9 eV). Inset are 97.5 % boundary surfaces of the corresponding molecular orbitals, with the atomic order O, C, S running left to right. Also plotted are $\cos^2\theta_{2D}$ values (black line, right axis) demonstrating the variation of the molecular axis distribution over time.

cross sections for these channels are anisotropic, with obvious increases in ionization propensity to the $\tilde{X}$-channel and $\tilde{A}$-channel in the antialigned configuration, and an increase in the $\tilde{C}$-channel yield when OCS is aligned parallel to the ionizing light polarization.

The integrated photoelectron intensity arising from ionization to the first four electronic states of OCS^+ as well as simulated ionization cross sections, both integrated over the specified photoelectron kinetic energy ranges, are plotted as a function of pump-probe time delay alongside 97.5 % boundary surfaces of the corresponding molecular orbitals in Fig. 1. Enlarged transparent isosurfaces displaying the orbital structure with respect to the molecular backbone are also presented in Fig. S2 in the ESI. The evolving axis distributions moments ($A^K_{Q,S}(t)$ parameters) of the rotational wavepacket were extracted from these time-dependent variations in cross-section using the method presented in Section III A and are presented in Fig. S3 in the Supplementary information. From this set of $A^K_{Q,S}(t)$ parameters it is possible account for the specific sample of molecules in the XUV probe measurement,[60] and we calculate a value of $\cos^2\theta_{3D}$ of 0.74 at the peak of the revival using the relationship $\cos^2\theta_{3D} = \frac{1}{3} + \frac{2}{3}A^2_{0,0}$. At the peak of the revival, truncating our $A^K_{Q,S}(t)$ parameters to $A^2_{0,0}$, we can estimate that around 55% of the molecules sampled have their axes aligned within a double cone subtending an angle of 30° from its central axis (cf. 33% for an unaligned sample) and 75% lie within an equivalent 45° cone, where the central axis of the cones is the laser polarization axis. Despite only using a single pulse for alignment, the level of alignment achieved is sufficient to resolve the higher angular momentum components of the PAD up to L=6.[24]

For the $\tilde{X}$-state continuum, both data and theory show a decrease in ionization propensity as the molecular axis distribution comes into alignment with the polarization vector of the ionizing light. As the $\tilde{X}$-state corresponds to the removal of an electron from the HOMO 3π orbital, which is shown inset in Fig. 1, this observation is consistent with the presence of the node along the molecular axis in an orbital of π symmetry. Ionization to the $\tilde{A}$-state of OCS^+ corresponds to the removal of an electron from the 2π bonding orbital. The delay-dependent integrated photoelectron intensity (solid blue line) therefore behaves similarly to that of the $\tilde{X}$-state channel in that the propensity for ionization into the $\tilde{A}$-state decreases as the molecular axis distribution becomes more aligned with the polarization of the ionizing light. The simulated ionization cross sections are consistent with the experimental observations though underestimate the experimentally observed variation in yield. Given the long vibrational progression associated with the $\tilde{A}$-band, it is possible that static minimum energy geometry calculations do not describe the full complexity of the ionization dynamics at play, see section IV C for full discussion.

Ionization into the $\tilde{B}$-state of OCS^+ corresponds to the removal of an electron from the 9σ orbital. In this case, the agreement between the changes in cross section with alignment in data and theory in Fig. 1 appears poor, with the data (solid blue line) showing an apparent significant decrease in cross section with increasing alignment with

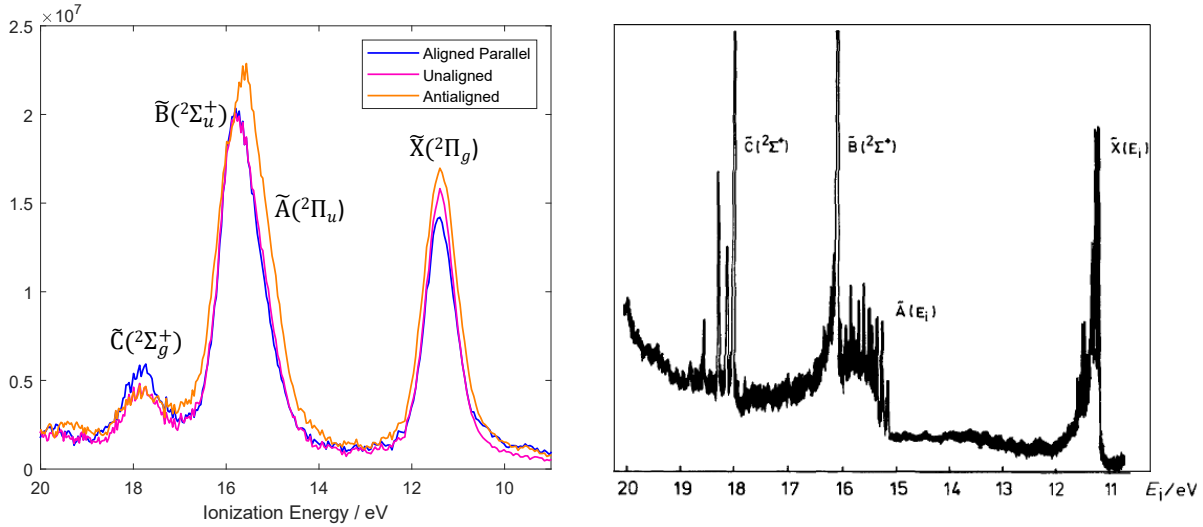

FIG. 2. Left: Plots of experimental photoelectron spectra of OCS at 23.6 eV from the current work. The magenta line corresponds to the photoelectron spectrum of randomly oriented OCS molecules. The blue and orange lines correspond to pump-probe spectra at the maximum of the first revival of OCS (40.5 ps delay) with the alignment pulse polarization aligned parallel and perpendicular to the ionizing light polarization, respectively. Right: 21 eV photoelectron spectrum of OCS reproduced with permission from reference 59.

the ionizing light, while the theory (dashed blue line) predicts a very slight increase in cross section consistent with ionization from a σ-orbital. This can be understood when looking at the energies and Franck-Condon envelopes of the transitions to the $\tilde{A}$-state and $\tilde{B}$-states of OCS^+, shown in Fig. 2. The $\tilde{A}$- and $\tilde{B}$-states are very close together in energy, however, while the transition from the neutral ground state of OCS to the $\tilde{B}$-state of OCS^+ is largely vertical, giving rise to a large origin peak and relatively few additional vibronic bands, ionization to the $\tilde{A}$-state gives rise to a broad Franck-Condon envelope indicative of a large change in the equilibrium geometry upon ionization to this state, consistent with the bonding character of the 2π-orbital. Thus, while some of the vibronic bands on the low binding energy edge of the $\tilde{A}$-state may be isolated with little contamination from the $\tilde{B}$-state signal, the $\tilde{B}$-state cannot be isolated from the $\tilde{A}$-state band. The large changes in the $\tilde{A}$-state cross section therefore dominate leading to apparent anomalous behaviour in the ionization yield data.

The $\tilde{C}$-channel of OCS corresponds to the removal of an electron from the 8σ orbital. The experimental integrated yield for ionization to this state in Fig. 1 is weak compared with the first 3 ionization channels, see Fig. 2 for comparison, and therefore the modulation of the photoelectron yield with alignment is on a similar order to our experimental error for this channel. Despite this, we observe an increasing photoionization yield with increasing alignment with the ionizing light polarization at around 40.5 ps delay which is in good quantitative agreement with the theory, which predicts a similar scale for the variation in cross section with alignment.

C. Laboratory Frame PADs of OCS in the range $h\nu = 20.5 - 24$ eV

The minimum energy geometry ePolyScat β_2 anisotropy parameters for the first four ionization channels in the range 0 - 30 eV eKE are presented alongside experimental values from the current work and the synchrotron measurements from references 28 and 29 in Fig. 3. The experimental and ePolyscat values of the β_2 anisotropy parameter for the first four ionization channels of randomly oriented OCS molecules at $h\nu$ = 20.5 eV and 23.6 eV are presented with synchrotron measurements at $h\nu$ = 21.2 eV and 24 eV from reference 29 in Table S1 in the ESI. The experimental values of β_2 for the $\tilde{X}$-channel at $h\nu$ = 20.5 eV and 23.6 eV are consistent with the synchrotron data in this photon energy range c.f. 1.60 ± 0.10 at 23.6 eV in the current work and 1.30 ± 0.07 at 24.0 eV in reference 29; we attribute the small discrepancy in values to differences in the selected eKE ranges for integration as we observe vibronic effects on the magnitude of β_2 within this peak such that integrating over the basewidth decreases the average value of β_2.

The experimental angular distribution parameters demonstrate that the ionization transition to the $\tilde{X}$-state of OCS^+ gives rise to a photoelectron distribution with strong anisotropy parallel to the laser polarization at $h\nu$ = 20.5 eV - 24.0 eV, as the β_2 value is large and positive in this kinetic energy range. The values of β_2 are also increasing with increasing photon energy in both the current work and the synchrotron measurements. ePolyScat predicts a more isotropic angular distribution, providing an unaligned β_2 value of 1.0 at $h\nu$ = 20.5 eV which decreases to 0.85 eV as the photon energy increases to 23.6 eV. When comparing the β_2 values in the synchrotron

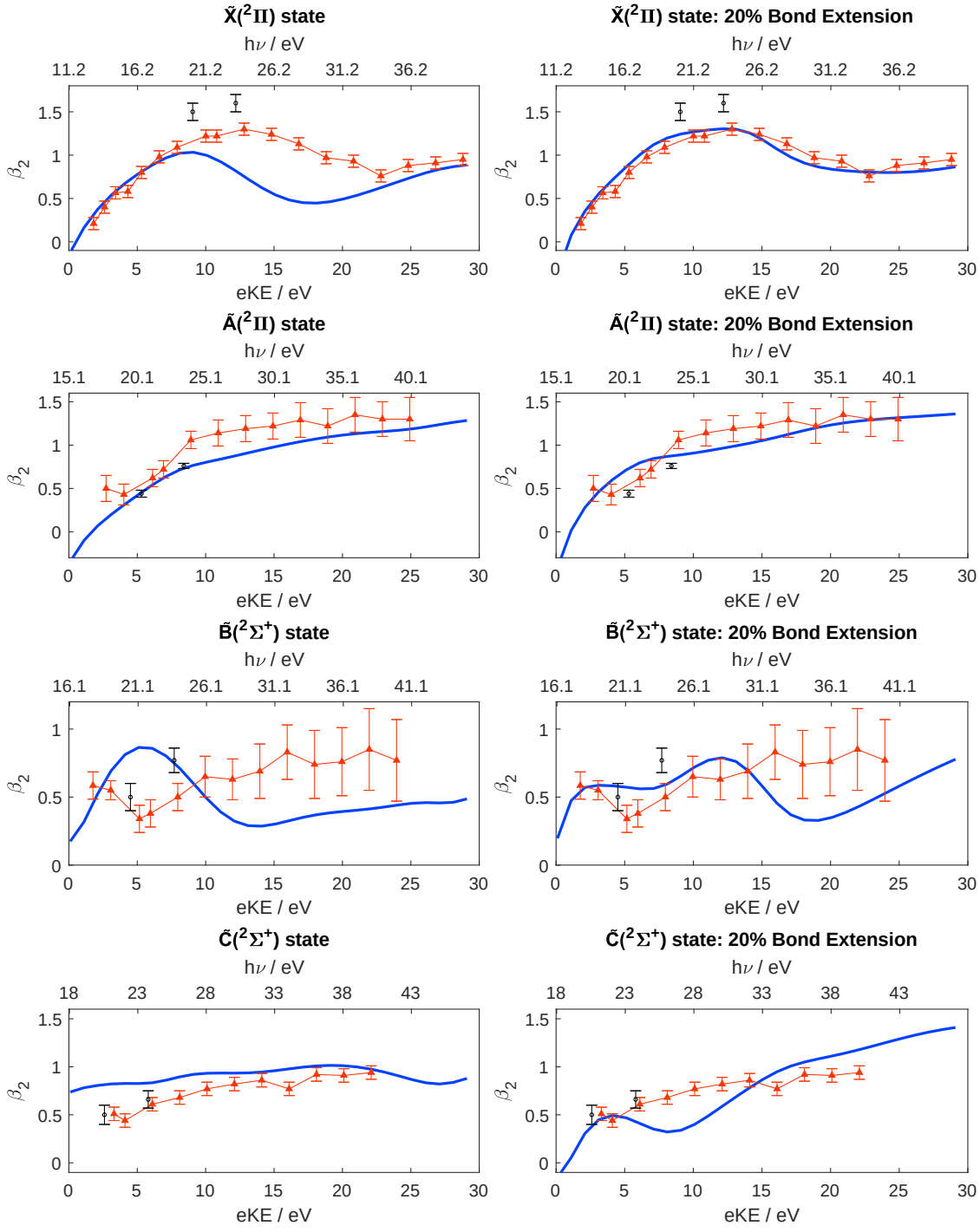

FIG. 3. Calculated β_2 parameters for the first four ionization channels of OCS as a function of electron kinetic energy (blue lines) at the minimum energy geometry (left) and for OCS elongated by 20% relative to the ground state equilibrium geometry as a function of electron kinetic energy (right). This extension corresponds to an increase in bond length from 1.569 Å to 1.854 Å for C−S, and 1.131 Å to 1.386 Å for C−O. Computational values are plotted against experimental values from the current work (black points) and from references 28 and 29 (orange triangles).

data and theory over a broad range of electron kinetic energies, it can be seen that there is a significant decrease with increasing eKE, which reaches a minimum at 22 eV eKE in the data from ref. 29 and at 16 eV eKE in the theory. This decrease results from a Cooper minimum due to the large contribution of the sulfur $3p$ orbital to the 3π molecular orbital. We therefore attribute the difference in the magnitude and trend in β_2 in the data vs. theory to the difference in the scale of the effect of the Cooper minimum on the value of β_2.

Given that the experimental photoelectron spectrum from Kovač *et al.* shows significant vibrational progressions in both the C−O and C−S stretches for ionization to the $\tilde{X}$-state,[59] it is possible that the greatest Franck-Condon probability does not lie at the minimum energy geometry of the ground vibrational state. Previous calculations appear to suggest that bond length changes are anticorrelated for ionization into the first four electronic states of OCS^+.[50] However, for the $\tilde{X}$-state, only a minimal change in one bond length is observed - i.e. the C−S bond length is increased by 0.09 Å accompanied by a negligible change in the C−O bond distance (-0.03 Å). Looking in more detail at the results of the calculations concerning the $\tilde{A}$-state, these also showed significant changes in the C−O bond distances only, disagreeing with the experimental photoelectron spectrum of OCS that has significant progressions in both C−O and C−S stretches in the $\tilde{A}$-band. In fact, the first three states have significant progressions in both C−O and C−S stretches, while the $\tilde{C}$–state appears to have only a significant change to the C−O bond length experimentally. The previous experimental observations in the literature therefore appear at odds with the calculation of Takeshita et al., suggesting a model involving a symmetrical stretch may better describe the average geometry change for the first three ionization channels. Therefore, to investigate the sensitivity of the simulation to these small-scale molecular geometry changes, we have calculated ePolyScat β_2 parameters as we symmetrically stretch the C−O and C−S bonds, which are presented in Fig. S4 in the ESI alongside the experimental data from references 28 and 29. This scan reveals that the scale of the contribution of the Cooper minimum is sensitive to even picometer-scale molecular geometry changes such that vibrational motion would lead to changes in the magnitude of its effect on the PAD at a given wavelength, highlighting the importance of careful consideration of the envelope of vibrational states that may be occupied for a given set of experimental conditions when modelling experimental data. We reiterate here that the changes in structure expected are ionization channel dependent and may not be fully symmetric. A full-scale exploration of the effects of such changes for all ionization channels and potential structures is beyond the scope of the current work but is a critical consideration for further analysis. In general, the vibrational dependence of PADs is complicated, and generally signifies a breakdown of the Franck-Condon approximation; such effects are expected to be pronounced in regions with strong continuum resonances and/or channel couplings. See, for examples, work from Poliakoff, Lucchese and co-workers who have investigated these types of effect in a range of small molecules.[61–63]

Of the molecular geometries sampled in the scan, the magnitude of the effect of the Cooper minimum on the β_2 parameters observed in the data from references 28 and 29 is best reproduced by ePolyScat for a symmetric bond extension of 20% from the calculated minimum energy geometry, corresponding to an increase in bond length from 1.569 Å to 1.854 Å for C−S, and 1.131 Å to 1.386 Å for C−O, see Fig. 3. Given that ionization to the ground vibrational level of the cation $\tilde{X}$-state has been theoretically predicted to give rise to an increase in the C−S bond length of 0.086 Å,[50] these results are consistent with a single-channel model of photoionization proving sufficient in this case, when taking into account vibrational averaging due to the non-static nature of the molecular geometry and sampling over the full FC progressions in the stretching modes, see Fig. 2 and Refs. [50, 51]); though we note the possibility of a slight overestimate of the depth of the scattering potential for heavy atoms at the current level of (non-relativistic) electronic structure theory (see, for instance, discussion in Ref. 38) which may lead to an overestimate of the bond length changes.

Ionization into the $\tilde{A}$-state gives rise to a parallel anisotropic distribution that becomes increasingly anisotropic with increasing photon energy in the 20.5 eV - 24.0 eV range in both the current data and synchrotron measurements (see Fig. 3 and Table S1 in the ESI). The current measurements seem to suggest a less anisotropic distribution than the synchrotron data (c.f. $\beta_2 = 0.76$ at 23.6 eV in the current measurements vs $\beta_2 = 1.06$ at 24.0 eV in the sychrotron data from reference 29), however, this difference could be due to the difficulty deconvolving the signals from the overlapped $\tilde{A}$- and $\tilde{B}$-channels. For the $\tilde{A}$-channel, ePolyScat is in agreement with the experimental values of β_2 from the current work c.f. 0.43 and 0.44 ± 0.04 respectively at 20.5 eV and 0.73 and 0.76 ± 0.03 respectively at 23.6 eV. Given the relative lack of structure in the $\tilde{A}$-state continuum, the predicted trends in β_2 as a function of eKE are equivalent for the minimum energy geometry and stretched molecular geometry (see Fig. 3). The main change associated with elongation of the bonds is an increase in the magnitude of the β_2 values across the whole eKE range calculated, bringing the values into closer agreement with the synchrotron measurements from reference 29 e.g. at 24 eV the ePolyscat value increases from 0.73 at the minimum energy geometry to 0.87 at the elongated geometry (c.f. the experimental value of 1.06 ± 0.10). This indicates that the differences between the experimental and theoretical β_2 values could result from the comparison of theory at the minimum energy geometry to experimental values which are integrated over the full Franck-Condon envelope of the ionization channels in both the current experiment and reference 29, where ro/vibronic couplings

can induce changes in the symmetry of the photoelectron wavefunction and the sampling of molecular geometries will be sensitive to zero-point motion, the rovibrational temperature and Franck-Condon factors.

In the eKE range corresponding to the $\tilde{B}$-state channel, the β_2 values are positive (see Table S1 and Fig. 3), indicating electron emission predominantly along the polarization axis of the ionizing light. The emission becomes increasingly anisotropic with increasing photon energy. The synchrotron data shows larger differences in the measured values of β_2 for the $\tilde{A}$- and $\tilde{B}$-states than are observed in the present work, which is most likely due to the fact that we have significant overlap between the two signals at the resolution of the current experiment. Interestingly, however, our measurements are in quantitative agreement with the ePolyScat calculated β_2 parameters, which predict a value of 0.73 for the $\tilde{B}$-state, which is also very close to the predicted value of the $\tilde{A}$-state. Despite the increased error in the synchrotron experimental β_2 values for this channel, the geometric distortion again appears to improve agreement between the magnitudes and trends in the ePolyscat calculation relative to those from reference 29 e.g. at ∼24 eV the ePolyscat value decreases from 0.73 at the minimum energy geometry to 0.62 at the elongated geometry (c.f. the experimental value of 0.5 ± 0.1). The ePolyScat results at the minimum energy geometry demonstrate that the $\tilde{B}$-state continuum is highly structured, with a maximum in β_2 values at around 5 eV eKE, resulting from a shape resonance, and a minimum at around 13 eV eKE, resulting from a Cooper minimum due to the sulfur $3p_z$ contribution to the 9σ orbital. However, at the elongated geometry, the calculations show a less significant effect from the shape resonance such that the maximum in β_2 is no longer present.

Our experimental β_2 values for the $\tilde{C}$-state channel in Table S1 in the ESI, which show weak parallel anisotropy which increases with increasing eKE, are in agreement with the synchrotron data (e.g. 0.50 ± 0.10 at 20.5 eV from the current work vs 0.51 ± 0.07 at 21.2 eV from reference 29). The experimental values are consistent with the ePolyScat calculated β_2 values, while slightly more isotropic in experiment vs. theory (c.f. 0.50 ± 0.10 v.s. 0.80 respectively at 20.5 eV), see Fig. 3. At the elongated geometry the magnitude of the β_2 values decreases, e.g. at ∼24 eV the ePolyscat value decreases from 0.83 at the minimum energy geometry to 0.45 at the elongated geometry (c.f. the experimental values of 0.61 ± 0.07[29] and 0.66 ± 0.10 at 24 eV and 23.6 eV, respectively). Additionally, the calculated trend in β_2 with eKE at the minimum energy geometry is in good agreement with that observed in reference 29. At the elongated geometry the trend deviates from the relatively flat structure observed in the measurement, with the appearance of a minimum in β_2 at ∼9 eV eKE associated with the formation of a shape resonance. The strongest peaks in the vibrationally-resolved photoelectron spectrum from reference 59 correspond to the C−O stretch progression for the $\tilde{C}$-state, compared with the other states for which progressions are observed in both C−O and C−S stretches. This perhaps results in preferential sampling of geometries which are asymmetrically elongated along the C−O bond in the $\tilde{C}$-state continuum, leading to poorer agreement between the experimental data and the theoretical calculations using the simplified symmetrically stretched model in the case of this ionization channel.

D. Alignment Frame PADs of OCS at hν = 23.6 eV

The full set of the aligment-frame PADs presented in this section is available via Figshare.[64]

1. *The $\tilde{X}$ ionization channel*

The experimental and simulated alignment-frame angular distribution parameters arising from ionization to the $\tilde{X}$-state of OCS^+ integrated over the eKE range 11.7 eV - 12.8 eV are presented as a function of pump-probe time delay in the top and middle rows of Fig. 4, respectively. There are small differences between the β_2 values along the baseline of the time-dependent scan and the unaligned values of β_2 presented in Table S1 in the ESI. We have integrated over broader range of eKE values for the time-dependent measurements of the $\tilde{X}$-state in order to improve the s/n, however, this means integrating over a broader range of vibronic transitions, which is observed here to have an impact on the magnitude of β_2 but not on the time-dependent behaviour of this band. The decrease in the baseline value of β_2 can also in part be attributed to the long-lived alignment of the molecular axis distribution. The effect of the long-lived alignment is seen in the Coulomb explosion data, where a $\cos^2\theta_{2D}$ of around 0.58 is observed, c.f. 0.5 for an isotropic distribution of molecular axes. As the molecular axis distribution becomes increasingly aligned with the laser polarization, peaking at a delay time of 40.5 ps, the observed β_n parameters decrease (i.e. the PAD becomes more isotropic), or stay the same, indicating an overall greater propensity for electron emission perpendicular to the polarization of the ionizing light when the polarization is parallel to the molecular axis. This is supported by the ePSproc simulated alignment frame angular distributions for β_2 and β_6, however, for β_4 the opposite alignment-dependent behaviour is predicted in this kinetic energy range. ePSproc predicts an increase from $\beta_4 = 0$ at baseline to $\beta_4 = 0.058$ followed by a decrease to $\beta_4 = -0.051$ at the minimum, which should exceed our experimental error for our β_4 values ($\pm$ 0.02), but is not observed in the experimental data. This observation may be explained by the effect of the Cooper minimum being overestimated by the theory in this kinetic energy range. As the Cooper minimum results from the ionization of an atomic $3p$ orbital, this phase change would affect only the d-partial wave of the outgoing electron. The Cooper

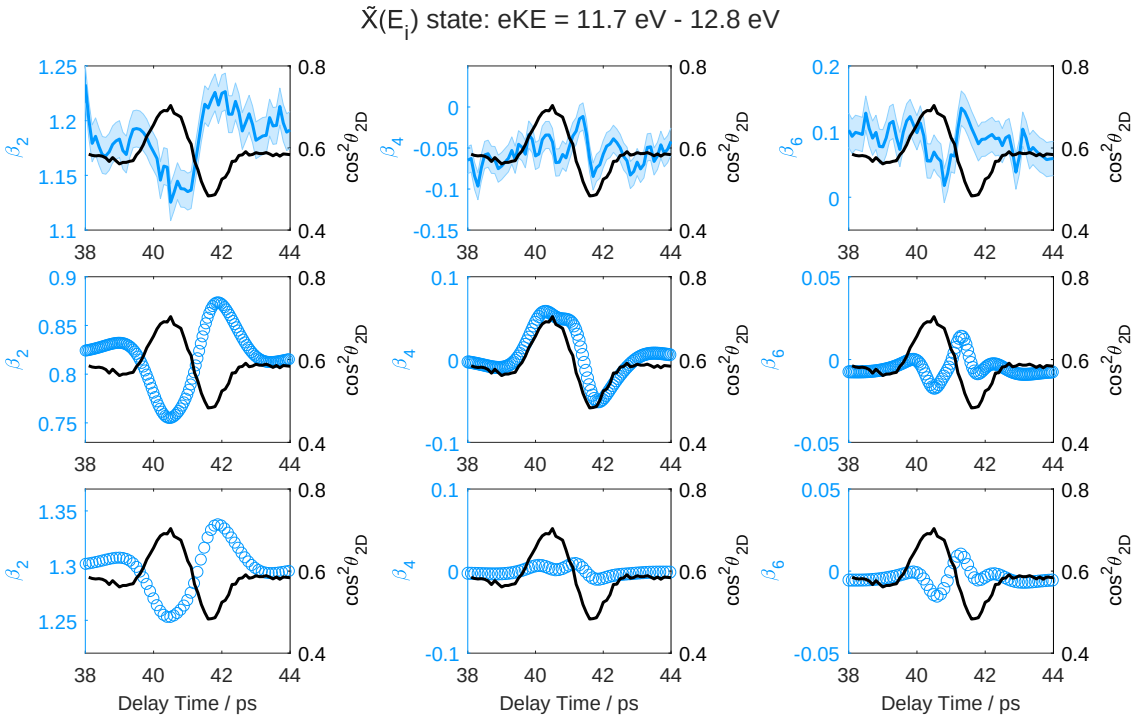

FIG. 4. Top row: Plots of experimental PAD parameters (β_2, β_4, β_6) as a function of pump-probe time delay. Values are averaged over the kinetic energy range 11.7 - 12.8 eV, which corresponds to the base-width of the $\tilde{X}$-state peak in the photoelectron spectrum. Middle Row: Plots of simulated PAD parameters expected to arise from photoionization to the $\tilde{X}$-state over the kinetic energy range of the experiment as a function of pump-probe time delay. Bottom row: Plots of simulated PAD parameters expected to arise from photoionization to the $\tilde{X}$-state for bond lengths symmetrically stretched by 20% from the ground state minimum over the kinetic energy range of the experiment as a function of pump-probe time delay. This extension corresponds to an increase in bond length from 1.569 Å to 1.854 Å for C−S, and 1.131 Å to 1.386 Å for C−O. Note that the axis scales are chosen to adequately display all features, and may not be equivalent. All data are plotted alongside the $\cos^2\theta_{2D}$ as a function of time measured by Coulomb explosion of OCS at 800 nm (black).

minimum therefore predominantly affects the agreement with the alignment-dependent trends in the experimental data in the β_4 component of the PAD, as the molecular axis alignment is increased and the higher angular momentum components of the distribution begin to be resolved.

The experimental alignment frame β_n parameters are presented alongside simulated angular distribution parameters for OCS with bonds stretched by 20% relative to the minimum energy geometry in the bottom row of Fig. 4. It can be seen from Fig. 4 that the agreement with our experimental data is improved at the elongated geometry, with the expected changes in β_4 now predicted to be smaller than 0.01, lower than our experimental error (± 0.02) and the magnitude of β_2 is more equivalent to the measurements ($\beta_2 \sim 1.3$ at baseline c.f. the experimental value of 1.17 ± 0.02). ePSproc alignment frame β_n parameters in the eKE range 0 - 30 eV for OCS at the minimum energy geometry and with bonds stretched by 20% relative to the minimum energy geometry are presented for molecular axis distributions corresponding to the baseline long-lived alignment and the maximum of the first revival are presented in Figs. S5 and S6 in the ESI, respectively. A comparison of these two plots demonstrates that the changes in β_4 expected from alignment are significantly decreased for the stretched molecular geometry, with a decreased effect of the Cooper minimum on the β_2 values also evident. From this we deduce that the observed effect of the Cooper minimum is significantly mediated by changes to the molecular geometry and hence appears weaker in the experimental measurements relative to single-point theoretical predictions at the minimum energy geometry due to the non-static nature of the molecular geometry and vibrational averaging (as discussed in Section IV C).

2. *The* $\tilde{A}$ *ionization channel*

The experimental and simulated PAD parameters arising from ionization to the $\tilde{A}$-state of OCS^+ over the photoelectron kinetic energy range 8.1 - 8.7 eV are presented as a function of pump-probe time delay in Fig. 5. The values of β_2 and β_4 are observed to decrease with increasing alignment with the ionizing light polarization, with β_2 reducing from 0.68 ± 0.02 to 0.52 ± 0.02 and

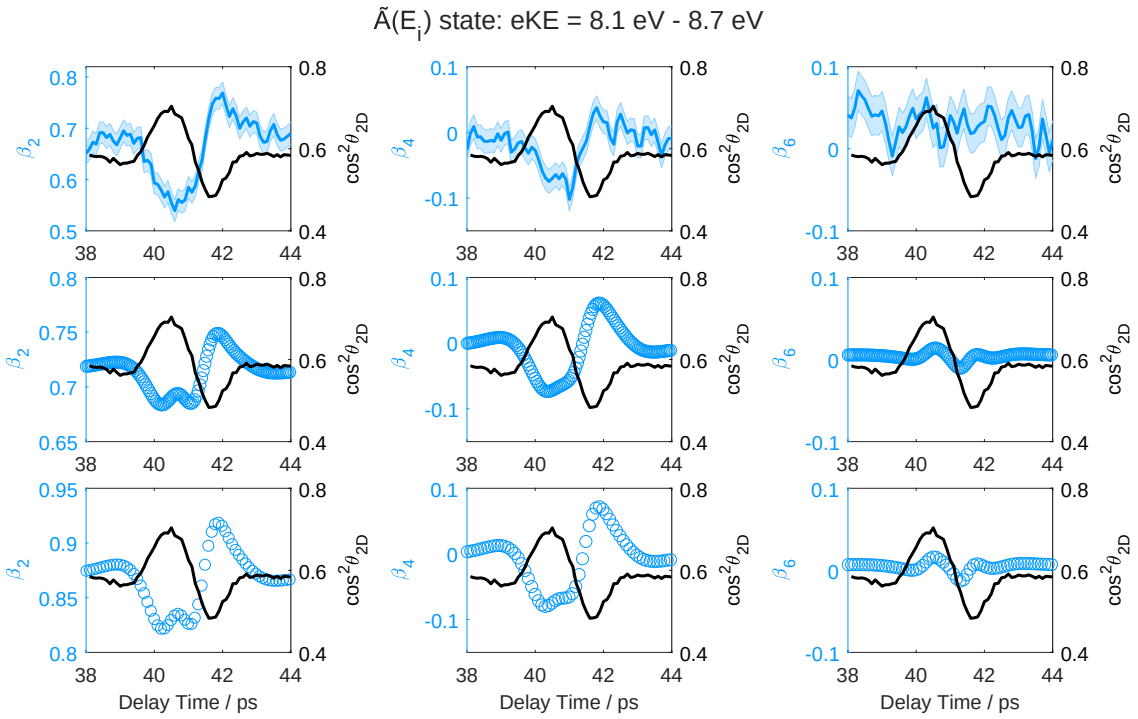

FIG. 5. Top row: Plots of experimental PAD parameters (β_2, β_4, β_6) as a function of pump-probe time delay. Values are averaged over the kinetic energy range specified which corresponds to the Ã-state in the photoelectron spectrum. Middle Row: Plots of simulated PAD parameters expected to arise from photoionization to the Ã-state over the kinetic energy range of the experiment as a function of pump-probe time delay. Bottom row: Plots of simulated PAD parameters expected to arise from photoionization to the Ã-state for bond lengths symmetrically stretched by 20% from the ground state minimum over the kinetic energy range of the experiment as a function of pump-probe time delay. This extension corresponds to an increase in bond length from 1.569 Å to 1.854 Å for C−S, and 1.131 Å to 1.386 Å for C−O. Note that the axis scales are chosen to adequately display all features, and may not be equivalent. All data are plotted alongside the $\cos^2\theta_{2D}$ as a function of time measured by Coulomb explosion of OCS at 800 nm (black).

β_4 reducing from 0.00 ± 0.02 to -0.10 ± 0.02. The experimental magnitudes and alignment frame fluctuations in β_2 and β_4 are well reproduced by the ePSproc calculations at the minimum energy geometry, with only a slight underestimation in the magnitude of the variation in β_2 with alignment, which could result from geometric sampling effects, indicating that both the ionization process and alignment distribution are well described by the theory. Very small changes are predicted by the ePSproc calculations for the value of β_6, however, these are not observable in the data as these changes are smaller than our statistical error for the measured β_6 parameters (± 0.02). Similarly to the X̃-state, the baseline value of β_2 is decreased in the time-resolved measurements relative to the spectrum of unaligned OCS integrated over the same eKE range (0.68 ± 0.02 vs. 0.76 ± 0.03, respectively), which we attribute to the effect of long-lived alignment of the molecular axis distribution. The broad eKE range simulations for the β_n parameters for ionization to the Ã-state of OCS^+ in Fig. S7 in the ESI show no strong fluctuations indicating no significant contributions from shape resonances or Cooper minima in this continuum in this eKE range, consistent with the observations in reference 29. From this, we predicted that the time-evolution of the alignment-frame PAD would be less sensitive to symmetric geometry changes than for continua where significant contributions from shape resonances or Cooper minima are observed at the minimum energy geometry. The broad eKE range simulations for the alignment frame β_n parameters for the elongated geometry in Fig. S8 of the ESI, and the simulated time-dependence of the alignment frame PAD presented in the bottom row of Fig. 5, demonstrate that the lack of continuum structure persists at the elongated geometry and as a result the only significant change observed in the PAD at the elongated geometry is the increase in the magnitude of β_2 discussed in Section IV C, supporting this hypothesis. Concomitant with the increase in β_2 at the elongated geometry, there is an increase in the predicted variation in the magnitude of β_2 with alignment, indicating that the large scale of variation in β_2 experimentally results, at least in part, from averaging over the vibronic structure of the Ã- ionization channel, while the experimentally measured magnitude of β_2 is reduced by the overlap with the B̃- ionization channel in the current experiment, see Section IV D 3.

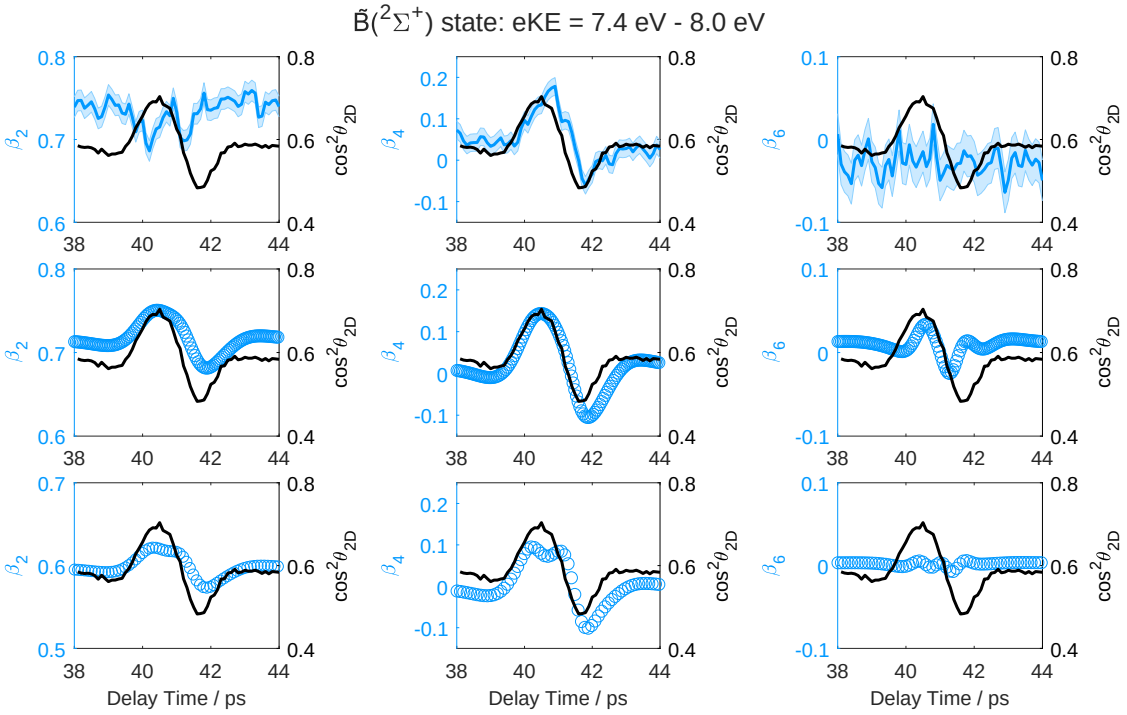

FIG. 6. Top row: Plots of experimental PAD parameters (β_2, β_4, β_6) as a function of pump-probe time delay. Values are averaged over the kinetic energy range specified which corresponds to the B̃-state in the photoelectron spectrum. Middle Row: Plots of simulated PAD parameters expected to arise from photoionization to the B̃-state over the kinetic energy range of the experiment as a function of pump-probe time delay. Bottom row: Plots of simulated PAD parameters expected to arise from photoionization to the B̃-state for bond lengths symmetrically stretched by 20% from the ground state minimum over the kinetic energy range of the experiment as a function of pump-probe time delay. This extension corresponds to an increase in bond length from 1.569 Å to 1.854 Å for C−S, and 1.131 Å to 1.386 Å for C−O. Note that the axis scales are chosen to adequately display all features, and may not be equivalent. All data are plotted alongside the $\cos^2\theta_{2D}$ as a function of time measured by Coulomb explosion of OCS at 800 nm (black).

3. *The* B̃ *ionization channel*

The angular distribution parameters arising from ionization to the B̃-state of OCS^+ are presented alongside simulated angular distribution parameters over kinetic energy range 7.4 - 8.0 eV as a function of pump-probe time delay in Fig. 6. Despite the significant overlap of the B̃-state with the Ã-state, we are able to resolve state-specific alignment-dependent changes in the β_4 parameter with remarkable agreement between experiment and theory, observing an increase in β_4 with increasing alignment for the B̃-channel c.f. decreasing anisotropy in the Ã state channel. The observation of state specific behaviour in the B̃-channel PAD, contrasts with our observations in the photoelectron yield, where the variations in the Ã-channel signal dominated. The β_2 parameters are observed to remain approximately constant across the full delay range, which could result from destructive interference between the opposing time-dependent changes in the β_2 values of the photoelectron distributions arising from each channel, or coupling between the two states; the minor structure visible between 40 and 41.5 ps appears to indicate the former. Changes in the β_6 parameter are not observed in this case as the changes are predicted to be on the order of 0.02 which is on the order of our statistical error (± 0.02).

The simulated time-dependence of the alignment frame PAD for ionization from the elongated geometry is presented in the bottom row of Fig. 6. The effect of the symmetric geometry change is small, there is a slight decrease in the magnitude of β_2 (0.6 at baseline vs. 0.72 at baseline at the minimum energy geometry) and the time-dependent variations of the β_2 and β_6 values are smaller also at the elongated geometry, improving agreement with the experimental observations in both cases. The broad eKE range simulations for the alignment frame β_n parameters for the minimum energy and elongated geometries are presented in Figs. S9 and S10 of the ESI, respectively. The simulated AFPADs demonstrate that at the minimum energy geometry there are reductions in β_4 and β_6 at around 5 eV consistent with a shape resonance which is not observed at the elongated geometry. Similarly, the effect of the Cooper minimum can be seen as a change in phase of the β_4 component of the PAD over the 10 - 20 eV eKE range at the minimum energy geometry, which is also absent in the calculations for the

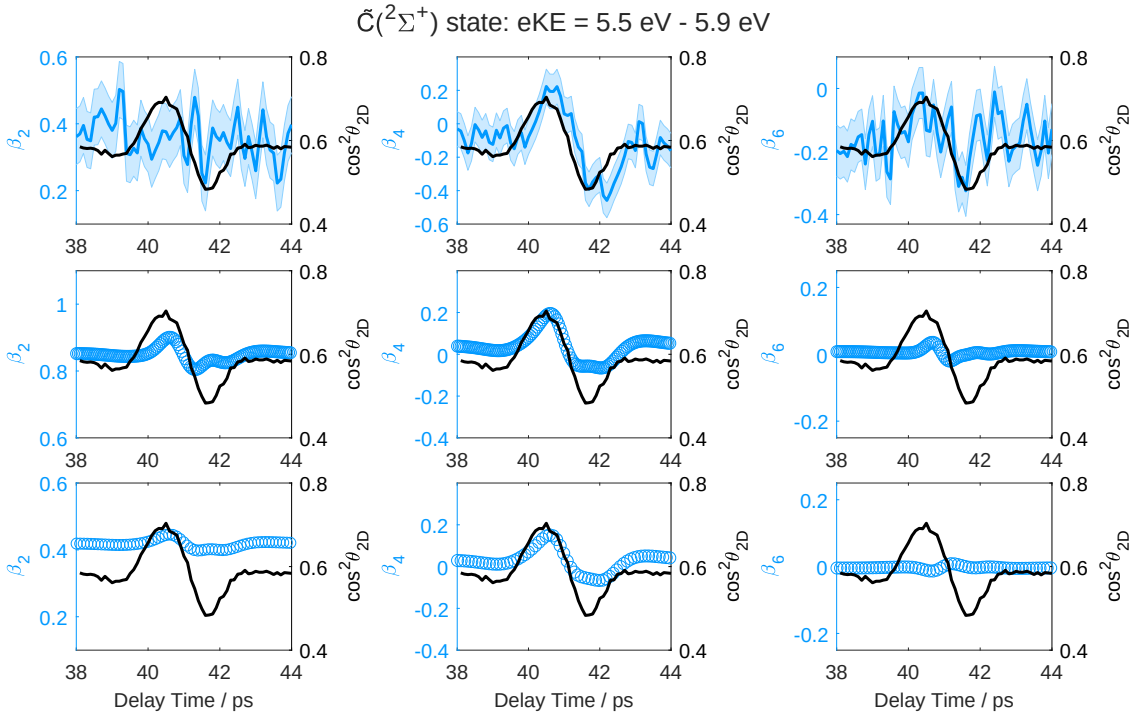

FIG. 7. Top row: Plots of experimental PAD parameters (β_2, β_4, β_6) as a function of pump-probe time delay (blue). Values are averaged over the kinetic energy range specified which corresponds to the base-width of the $\tilde{C}$-state peak in the photoelectron spectrum. Middle Row: Plots of simulated PAD parameters expected to arise from photoionization to the $\tilde{C}$-state over the kinetic energy range of the experiment as a function of pump-probe time delay. Bottom row: Plots of simulated PAD parameters expected to arise from photoionization to the $\tilde{C}$-state for bond lengths symmetrically stretched by 20% from the ground state minimum over the kinetic energy range of the experiment as a function of pump-probe time delay. This extension corresponds to an increase in bond length from 1.569 Å to 1.854 Å for C−S, and 1.131 Å to 1.386 Å for C−O. Note that the axis scales are chosen to adequately display all features, and may not be equivalent. All data are plotted alongside the $\cos^2\theta_{2D}$ as a function of time measured by Coulomb explosion of OCS at 800 nm (black).

elongated geometry. These observations again indicate that vibrational motion may have a significant effect on the continuum structure, however, only has a small effect on the agreement with our experimental measurements in this case due to the relatively small impact of these structural features over the eKE range of this experiment.

4. *The $\tilde{C}$ ionization channel*

The PAD arising from ionization to the $\tilde{C}$-state of OCS^+ at 23.6 eV is presented alongside simulated angular distribution parameters over the same photoelectron kinetic energy range as a function of pump-probe time delay in Fig. 7. In this case, ePSproc predicts an increase in all of the β_n parameters with increasing alignment. Given the relative weakness of the $\tilde{C}$-channel peak, the statistical error is larger for this channel (± 0.08 for β_2) and therefore the very small changes in β_2 (on the order of 0.06) that are predicted by ePSproc cannot be seen in the data. Despite the higher level of noise here, we clearly observe very large changes in the β_4 parameter as a function of alignment (on the order of 0.70 ± 0.08). This increase in β_4 is predicted by ePSproc, though on a smaller magnitude than we observe in the data. For β_6, ePSproc once again predicted smaller changes than we see in the data, where we are able to pick out increases in magnitude with increasing alignment despite the low s/n associated with this peak.

The simulated time-dependence of the alignment frame PAD for ionization from the elongated geometry is presented in the bottom row of Fig. 7. The effect of the symmetric geometry change is most pronounced in β_2 (0.4 at baseline vs. 0.85 at baseline at the minimum energy geometry), which is very close to the experimentally observed value ($\beta_2 = 0.38 \pm 0.08$ at baseline experimentally). The time-dependent variation in β_2 is also reduced, seemingly in improved agreement with the experimental observations. However, while being small, the variation in β_6 values is now observed to have the opposite behaviour at the elongated geometry to that at the minimum energy geometry and that observed experimentally.

By comparison of the broad eKE range alignment frame PADs in Figs. S11 and S12 in the ESI, it becomes clear that the resonance at the elongated geom-

etry, which is not observed at the minimum energy geometry or in the synchrotron data, results in a change of sign of β_6, despite only contributing weakly in this eKE range, as its relative contribution is higher for the higher angular momenta. This demonstrates the importance of measuring the higher angular-momentum contributions to the PAD to correctly identify the effect of molecular structure on the ionization and scattering dynamics. The improved agreement between the experimentally observed magnitude of β_2 and the theoretical value at the elongated geometry indicates that vibrational motion is impacting the experimental values. However, agreement is not improved overall in the case of the $\tilde{C}$-band, which likely results from the difference in the vibronic structure of this band when compared to the three lowest ionization channels, causing poorer agreement with the symmetrically stretched geometry model through the formation of the shape resonance in this simplified model, see discussion in IV C.

V. CONCLUSIONS

We have presented experimental measurements and theoretical calculations of alignment frame PADs for the first four cation states of OCS. The level of alignment achieved has also allowed us to observe changes to the higher angular momentum components of the PAD (up to β_6) which are quantitatively compared to theoretical calculations. Theoretical molecular frame PADs are combined with experimentally derived alignment distribution moments, which define the spatial distribution of the measured ensemble, in order to produce theoretical alignment frame PADs that provide direct quantitative comparison to the experimental PADs. By monitoring multiple angular momentum components of the PADs across multiple different ionization channels we have a rigorous test of theory. Using a simple model of two molecular geometries we have demonstrated that the alignment dependent changes observed in the measurements show sensitivity to ro/vibronic couplings and geometric sampling. This is particularly apparent in regions of complex continuum structure such as Cooper minima and shape resonances where even picometer-scale changes in geometry lead to significant changes in the observed β_n's. The ability to quantitatively compare experiment and theory provides new opportunities to test different theoretical methods against experimental results and consider previously ignored aspects which determine the accuracy of those models across different ionization channels and molecular systems. This combined methodology therefore provides a versatile way of studying geometry-sensitive continuum structural features for non-dissociative ionization processes which may not be studied in the recoil frame. Future theoretical developments to be explored include geometric effects such as state averaging over the possible vibronic transitions and molecular geometries for each individual ionization channel, as well as exploring potential electron correlation effects which are not included in the present model. Future application of these methods to different molecular systems will also test the versatility of the theoretical models used for photoelectron scattering.

ACKNOWLEDGEMENTS

The authors thank the STFC for access to the Artemis facility. RSM thanks the EPSRC (EP/R010609/1) and Leverhulme trust (RPG-2021-257) for financial support. KLR thanks the EPSRC for financial support (EP/R010447/1).

[1] K. L. Reid and J. G. Underwood, Extracting molecular axis alignment from photoelectron angular distributions, The Journal of Chemical Physics **112**, 3643 (2000).
[2] J. G. Underwood and K. L. Reid, Time-resolved photoelectron angular distributions as a probe of intramolecular dynamics: connecting the molecular frame and the laboratory frame, Journal of Chemical Physics **113**, 1067 (2000).
[3] T. Seideman, Time-resolved photoelectron angular distributions: Concepts, applications, and directions, Annual Review of Physical Chemistry **53**, 41 (2002).
[4] K. L. Reid, Photoelectron angular distributions., Annual review of physical chemistry **54**, 397 (2003).
[5] T. Suzuki, Femtosecond time-resolved photoelectron imaging, Annual Review of Physical Chemistry **57**, 555 (2006).
[6] S. Ramakrishna and T. Seideman, On the information content of time- and angle-resolved photoelectron spectroscopy, Journal of Physics B: Atomic, Molecular and Optical Physics **45**, 194012 (2012).
[7] P. Hockett, General phenomenology of ionization from aligned molecular ensembles, New Journal of Physics **17**, 023069 (2015).
[8] E. Shigemasa, J. Adachi, M. Oura, and A. Yagishita, Angular Distributions of 1sσ Photoelectrons from Fixed-in-Space N2 Molecules, Physical Review Letters **74**, 359 (1995).
[9] A. Landers, T. Weber, I. Ali, A. Cassimi, M. Hattass, O. Jagutzki, A. Nauert, T. Osipov, A. Staudte, M. H. Prior, H. Schmidt-Böcking, C. L. Cocke, and R. Dörner, Photoelectron Diffraction Mapping: Molecules Illuminated from Within, Physical Review Letters **87**, 013002 (2001).
[10] O. Geßner, A. M. Lee, J. P. Shaffer, H. Reisler, S. V. Levchenko, A. I. Krylov, J. G. Underwood, H. Shi, A. L. East, D. M. Wardlaw, E. T. Chrysostom, C. C. Hayden,

and A. Stolow, Femtosecond multidimensional imaging of a molecular dissociation, Science **311**, 219 (2006).

[11] T. Weber, L. Foucar, T. Jahnke, M. Schoeffler, L. Schmidt, M. Prior, and R. Doerner, The hydrogen molecule under the reaction microscope: Single photon double ionization at maximum cross section and threshold (doubly differential cross sections), Journal of Physics B: Atomic, Molecular and Optical Physics **50**, 10.1088/1361-6455/aa7e3b (2017).

[12] K. A. Larsen, C. S. Trevisan, R. R. Lucchese, S. Heck, W. Iskandar, E. Champenois, A. Gatton, R. Moshammer, R. Strom, T. Severt, B. Jochim, D. Reedy, M. Weller, A. L. Landers, J. B. Williams, I. Ben-Itzhak, R. Dörner, D. Slaughter, C. W. McCurdy, T. Weber, and T. N. Rescigno, Resonance signatures in the body-frame valence photoionization of CF4, Physical Chemistry Chemical Physics **20**, 21075 (2018).

[13] S. Heck, A. Gatton, K. A. Larsen, W. Iskandar, E. G. Champenois, R. Strom, A. Landers, D. Reedy, C. Dailey, J. B. Williams, T. Severt, B. Jochim, I. Ben-Itzhak, R. Moshammer, R. Dörner, D. S. Slaughter, and T. Weber, Symmetry breaking in the body-fixed electron emission pattern due to electron-retroaction in the photodissociation of H2+ and D2+ close to threshold, Physical Review Research **1**, 1 (2019).

[14] A. Sanchez, K. Amini, S. J. Wang, T. Steinle, B. Belsa, J. Danek, A. T. Le, X. Liu, R. Moshammer, T. Pfeifer, M. Richter, J. Ullrich, S. Gräfe, C. D. Lin, and J. Biegert, Molecular structure retrieval directly from laboratory-frame photoelectron spectra in laser-induced electron diffraction, Nature Communications **12**, 1 (2021).

[15] I. Vela-Peréz, F. Ota, A. Mhamdi, Y. Tamura, J. Rist, N. Melzer, S. Uerken, G. Nalin, N. Anders, D. You, M. Kircher, C. Janke, M. Waitz, F. Trinter, R. Guillemin, M. N. Piancastelli, M. Simon, V. T. Davis, J. B. Williams, R. Dörner, K. Hatada, K. Yamazaki, K. Fehre, P. V. Demekhin, K. Ueda, M. S. Schöffler, and T. Jahnke, High-energy molecular-frame photoelectron angular distributions: a molecular bond-length ruler, Physical Chemistry Chemical Physics , 13784 (2023), arXiv:2105.11897.

[16] J. B. Williams, C. S. Trevisan, M. S. Schöffler, T. Jahnke, I. Bocharova, H. Kim, B. Ulrich, R. Wallauer, F. Sturm, T. N. Rescigno, A. Belkacem, R. Dörner, T. Weber, C. W. McCurdy, and A. L. Landers, Imaging polyatomic molecules in three dimensions using molecular frame photoelectron angular distributions, Physical Review Letters **108**, 233002 (2012).

[17] H. V. S. Lam, S. Yarlagadda, A. Venkatachalam, T. N. Wangjam, R. K. Kushawaha, C. Cheng, P. Svihra, A. Nomerotski, T. Weinacht, D. Rolles, and V. Kumarappan, Angle-dependent strong-field ionization and fragmentation of carbon dioxide measured using rotational wave packets, Physical Review A **102**, 43119 (2020).

[18] P. Hockett, M. Staniforth, K. L. Reid, and D. Townsend, Rotationally resolved photoelectron angular distributions from a nonlinear polyatomic molecule, Physical Review Letters **102**, 253002 (2009).

[19] Y. Tang, Y. I. Suzuki, T. Horio, and T. Suzuki, Molecular frame image restoration and partial wave analysis of photoionization dynamics of NO by time-energy mapping of photoelectron angular distribution, Physical Review Letters **104**, 073002 (2010).

[20] H. Stapelfeldt and T. Seideman, Colloquium: Aligning molecules with strong laser pulses, Reviews of Modern Physics **75**, 543 (2003).

[21] C. P. Koch, M. Lemeshko, and D. Sugny, Quantum control of molecular rotation, Reviews of Modern Physics **91**, 35005 (2019), arXiv:1810.11338.

[22] P. Hockett, *Quantum Metrology with Photoelectrons, Volume 2: Applications and Advances* (IOP Publishing, 2018).

[23] C. Marceau, V. Makhija, D. Platzer, A. Yu. Naumov, P. B. Corkum, A. Stolow, D. M. Villeneuve, and P. Hockett, Molecular Frame Reconstruction Using Time-Domain Photoionization Interferometry, Physical Review Letters **119**, 083401 (2017).

[24] K. L. Reid, Accessing the molecular frame through strong-field alignment of distributions of gas phase molecules, Philosophical Transactions of the Royal Society A: Mathematical, Physical and Engineering Sciences **376**, 20170158 (2018).

[25] M. Gregory, P. Hockett, A. Stolow, and V. Makhija, Towards molecular frame photoelectron angular distributions in polyatomic molecules from lab frame coherent rotational wavepacket evolution, Journal of Physics B: Atomic, Molecular and Optical Physics **54**, 145601 (2021), arXiv:2012.04561.

[26] P. Hockett and V. Makhija, Topical Review: Extracting molecular frame photoionization dynamics from experimental data, Journal of Physics B: Atomic, Molecular and Optical Physics **56**, 112001 (2023), arxiv:2209.04301 [physics, physics:quant-ph].

[27] D. Dill, Fixed-molecule photoelectron angular distributions, The Journal of Chemical Physics **65**, 1130 (1976).

[28] T. A. Carlson, M. O. Krause, F. A. Grimm, J. D. Allen, D. Mehaffy, P. R. Keller, and J. W. Taylor, Angle-resolved photoelectron spectroscopy of CS2 and COS measured with synchrotron radiation, The Journal of Chemical Physics **75**, 3288 (1981).

[29] T. A. Carlson, M. O. Krause, and F. A. Grimm, Angle resolved photoelectron spectroscopy of CS2 and COS measured as a function of photon energy from 21 to 70 eV, The Journal of Chemical Physics **77**, 1701 (1982).

[30] C. Bisgaard, O. Clarkin, G. Wu, and A. Lee, Time-resolved molecular frame dynamics of fixed-in-space CS2 molecules, Science **323**, 1464 (2009).

[31] S. Minemoto, H. Shimada, K. Komatsu, W. Komatsubara, T. Majima, S. Miyake, T. Mizuno, S. Owada, H. Sakai, T. Togashi, M. Yabashi, P. Decleva, M. Stener, S. Tsuru, and A. Yagishita, Time-resolved photoelectron angular distributions from nonadiabatically aligned CO2 molecules with SX-FEL at SACLA, Journal of Physics Communications **2**, 115015 (2018).

[32] E. Allaria, R. Appio, L. Badano, W. A. Barletta, S. Bassanese, S. G. Biedron, A. Borga, E. Busetto, D. Castronovo, P. Cinquegrana, S. Cleva, D. Cocco, M. Cornacchia, P. Craievich, I. Cudin, G. D'Auria, M. Dal Forno, M. B. Danailov, R. De Monte, G. De Ninno, P. Delgiusto, A. Demidovich, S. Di Mitri, B. Diviacco, A. Fabris, R. Fabris, W. Fawley, M. Ferianis, E. Ferrari, S. Ferry, L. Froehlich, P. Furlan, G. Gaio, F. Gelmetti, L. Giannessi, M. Giannini, R. Gobessi, R. Ivanov, E. Karantzoulis, M. Lonza, A. Lutman, B. Mahieu, M. Milloch, S. V. Milton, M. Musardo, I. Nikolov, S. Noe, F. Parmigiani, G. Penco, M. Petronio, L. Pivetta, M. Predonzani, F. Rossi, L. Rumiz, A. Salom, C. Scafuri, C. Serpico,

P. Sigalotti, S. Spampinati, C. Spezzani, M. Svandrlik, C. Svetina, S. Tazzari, M. Trovo, R. Umer, A. Vascotto, M. Veronese, R. Visintini, M. Zaccaria, D. Zangrando, and M. Zangrando, Highly coherent and stable pulses from the FERMI seeded free-electron laser in the extreme ultraviolet, Nature Photonics **6**, 699 (2012).

[33] J. Amann, W. Berg, V. Blank, F. J. Decker, Y. Ding, P. Emma, Y. Feng, J. Frisch, D. Fritz, J. Hastings, Z. Huang, J. Krzywinski, R. Lindberg, H. Loos, A. Lutman, H. D. Nuhn, D. Ratner, J. Rzepiela, D. Shu, Y. Shvyd'Ko, S. Spampinati, S. Stoupin, S. Terentyev, E. Trakhtenberg, D. Walz, J. Welch, J. Wu, A. Zholents, and D. Zhu, Demonstration of self-seeding in a hard-X-ray free-electron laser, Nature Photonics **6**, 693 (2012).

[34] F. Kelkensberg, A. Rouzée, W. Siu, G. Gademann, P. Johnsson, M. Lucchini, R. R. Lucchese, and M. J. Vrakking, XUV ionization of aligned molecules, Physical Review A - Atomic, Molecular, and Optical Physics **84**, 051404 (2011).

[35] A. Rouzée, F. Kelkensberg, W. K. Siu, G. Gademann, R. R. Lucchese, and M. J. J. Vrakking, Photoelectron kinetic and angular distributions for the ionization of aligned molecules using a HHG source, Journal of Physics B: Atomic, Molecular and Optical Physics **45**, 074016 (2012).

[36] A. Rouzée, P. Johnsson, L. Rading, A. Hundertmark, W. Siu, Y. Huismans, S. Düsterer, H. Redlin, F. Tavella, N. Stojanovic, A. Al-Shemmary, F. Lépine, D. M. Holland, T. Schlatholter, R. Hoekstra, H. Fukuzawa, K. Ueda, and M. J. Vrakking, Towards imaging of ultrafast molecular dynamics using FELs, Journal of Physics B: Atomic, Molecular and Optical Physics **46**, 164029 (2013).

[37] A. Rouzée, A. G. Harvey, F. Kelkensberg, D. Brambila, W. K. Siu, G. Gademann, O. Smirnova, and M. J. Vrakking, Imaging the electronic structure of valence orbitals in the XUV ionization of aligned molecules, Journal of Physics B: Atomic, Molecular and Optical Physics **47**, 124017 (2014).

[38] F. Brausse, M. J. J. Vrakking, and A. Rouzée, Shape resonances in angle-resolved photoionization of aligned CF3I molecules, Journal of Physics B: Atomic, Molecular and Optical Physics **56**, 075101 (2023).

[39] F. Frassetto, C. Cacho, C. A. Froud, I. E. Turcu, P. Villoresi, W. A. Bryan, E. Springate, and L. Poletto, Single-grating monochromator for extreme-ultraviolet ultrashort pulses, Optics Express **19**, 19169 (2011).

[40] M. Eckstein, C.-H. Yang, F. Frassetto, L. Poletto, G. Sansone, M. J. J. Vrakking, and O. Kornilov, Direct Imaging of Transient Fano Resonances in N_2 Using Time-, Energy-, and Angular-Resolved Photoelectron Spectroscopy, Physical Review Letters **116**, 163003 (2016).

[41] F. Rosca-Pruna and M. J. Vrakking, Experimental observation of revival structures in picosecond laser-induced alignment of I2, Physical Review Letters **87**, 153902 (2001).

[42] G. M. Roberts, J. L. Nixon, J. Lecointre, E. Wrede, and J. R. Verlet, Toward real-time charged-particle image reconstruction using polar onion-peeling, Review of Scientific Instruments **80**, 053104 (2009).

[43] V. Makhija, X. Ren, D. Gockel, A.-T. Le, and V. Kumarappan, Orientation Resolution through Rotational Coherence Spectroscopy, arXiv , 1 (2016), arxiv:1611.06476.

[44] X. Wang, A.-T. Le, Z. Zhou, H. Wei, and C. D. Lin, Theory of retrieving orientation-resolved molecular information using time-domain rotational coherence spectroscopy, Physical Review A **96**, 023424 (2017).

[45] P. Hockett and V. Makhija, *Quantum Metrology with Photoelectrons, Volume 3: Analysis Methodologies*, Quantum Metrology with Photoelectrons, Vol. 3 (IOP Publishing, 2023).

[46] G. M. J. Barca, C. Bertoni, L. Carrington, D. Datta, N. De Silva, J. E. Deustua, D. G. Fedorov, J. R. Gour, A. O. Gunina, E. Guidez, T. Harville, S. Irle, J. Ivanic, K. Kowalski, S. S. Leang, H. Li, W. Li, J. J. Lutz, I. Magoulas, J. Mato, V. Mironov, H. Nakata, B. Q. Pham, P. Piecuch, D. Poole, S. R. Pruitt, A. P. Rendell, L. B. Roskop, K. Ruedenberg, T. Sattasathuchana, M. W. Schmidt, J. Shen, L. Slipchenko, M. Sosonkina, V. Sundriyal, A. Tiwari, J. L. Galvez Vallejo, B. Westheimer, M. Włoch, P. Xu, F. Zahariev, and M. S. Gordon, Recent developments in the general atomic and molecular electronic structure system, The Journal of Chemical Physics **152**, 154102 (2020).

[47] M. W. Schmidt, K. K. Baldridge, J. A. Boatz, S. T. Elbert, M. S. Gordon, J. H. Jensen, S. Koseki, N. Matsunaga, K. A. Nguyen, S. Su, T. L. Windus, M. Dupuis, and J. A. Montgomery, General atomic and molecular electronic structure system, Journal of Computational Chemistry **14**, 1347 (1993).

[48] M. S. Gordon, Gamess website.

[49] G. Herzberg, *Molecular Spectra and Molecular Structure III: Electronic Spectra and Electronic Structure of Polyatomic Molecules* (Van Nostrand Reinhold Company, New York, USA, 1966).

[50] K. Takeshita, N. Shida, and E. Miyoshi, A theoretical study on the ionization of OCS with an analysis of vibrational structures of the photoelectron spectrum, Theoretical Chemistry Accounts **107**, 33 (2001).

[51] W. Chen, M. Hochlaf, P. Rosmus, G. Z. He, and C. Y. Ng, Vacuum ultraviolet pulsed field ionization-photoelectron study of OCS in the energy range of 15–19 eV, The Journal of Chemical Physics **116**, 5612 (2002).

[52] R. R. Lucchese, K. Takatsuka, and V. McKoy, Applications of the Schwinger variational principle to electron-molecule collisions and molecular photoionization, Physics Reports **131**, 147 (1986).

[53] F. A. Gianturco, R. R. Lucchese, and N. Sanna, Calculation of low-energy elastic cross sections for electron-CF4 scattering, The Journal of Chemical Physics **100**, 6464 (1994).

[54] A. P. P. Natalense and R. R. Lucchese, Cross section and asymmetry parameter calculation for sulfur 1s photoionization of SF[sub 6], The Journal of Chemical Physics **111**, 5344 (1999).

[55] R. R. Lucchese, ePolyScat User's Manual.

[56] P. Hockett, ePSproc: Post-processing suite for ePolyScat electron-molecule scattering calculations, Authorea 10.6084/m9.figshare.3545639 (2016), arxiv:1611.04043.

[57] P. Hockett, ePSproc: Post-processing for ePolyScat (Github repository), Github (2016).

[58] P. Hockett, V. Makhija, and J. Woodhouse, OCS alignment and photoionization calculations (2023).

[59] B. Kovač, The He I photoelectron spectra of CO2, CS2, and OCS: Vibronic coupling, The Journal of Chemical Physics **78**, 1684 (1983).

[60] J. Mikosch, C. Z. Bisgaard, A. E. Boguslavskiy, I. Wilkinson, and A. Stolow, The quantitative determination of laser-induced molecular axis alignment, Journal of Chemical Physics **139**, 10.1063/1.4812787 (2013).

[61] J. López-Domínguez, D. Hardy, A. Das, E. Poliakoff, A. Aguilar, and R. R. Lucchese, Mechanisms of Franck-Condon breakdown over a broad energy range in the valence photoionization of N2 and CO, Journal of Electron Spectroscopy and Related Phenomena **185**, 211 (2012).

[62] R. R. Lucchese, R. Montuoro, K. Kotsis, M. Tashiro, M. Ehara, J. D. Bozek, A. Das, A. Landry, J. Rathbone, and E. Poliakoff, The effect of vibrational motion on the dynamics of shape resonant photoionization of BF 3 leading to the state of, Molecular Physics **108**, 1055 (2010).

[63] G. J. Rathbone, E. D. Poliakoff, J. D. Bozek, and R. R. Lucchese, Intrachannel vibronic coupling in molecular photoionization, Canadian Journal of Chemistry **82**, 1043 (2004).

[64] J. Woodhouse, P. Hockett, and V. Makhija, OCS experimental AFPADs and theoretical AFPAD notebooks (2024).